Original Article

Diffusion MRI fiber diameter for muscle denervation assessment

Ek T. Tan^, Kelly C. Zochowski, Darryl B. Sneag

Department of Radiology and Imaging, Hospital for Special Surgery, New York, NY, USA

Contributions: (I) Conception and design: ET Tan, DB Sneag; (II) Administrative support: None; (III) Provision of study materials or patients: DB Sneag; (IV) Collection and assembly of data: ET Tan; (V) Data analysis and interpretation: All authors; (VI) Manuscript writing: All authors; (VII) Final approval of manuscript: All authors.

Correspondence to: Ek T. Tan, PhD. Hospital for Special Surgery, 535 East 70th Street, NY 10021, USA. Email: tane@hss.edu.

Background: To develop and evaluate a diffusion MRI-based apparent muscle fiber diameter (AFD) method in patients with muscle denervation. It was hypothesized that AFD differences between denervated, non-denervated and control muscles would be greater than those from standard diffusion metrics.

Methods: A spin-echo diffusion acquisition with multi-b-valued diffusion sampling was used. An orientation-invariant dictionary approach utilized a cylinder-based forward model and multi-compartment model for obtaining restricted and free fractions. Simulations were performed to determine precision, bias, and optimize dictionary parameters. In all, 18 exams of patients with muscle denervation and 8 exams of healthy subjects were performed at 3T. Six regions of interests (ROIs) within separate shoulder muscles were selected, yielding three groups consisting 47 control (healthy), 36 non-denervated (patients), and 68 denervated (patients) muscle ROIs. Two-sample *t*-tests (α=0.05) between groups were performed with Holm-Bonferroni correction. T_2- and fat fraction (FF)-mapping were acquired for comparison.

Results: Mean AFD was 89.7±13.6 μm in control, 71.6±15.3 μm in non-denervated, and 60.7±15.9 μm in denervated muscles and were significantly different (P<0.001) in paired comparisons and in 10/12 individual muscle region comparisons. Correlation between AFD and FF (–0.331, P<0.001) was low, but correlation between FA and FF was negligible (0.197, P=0.016). Correlation was low between AFD and T_2 (–0.395, P<0.001) and between FA and T_2 (0.359, P<0.001).

Conclusions: Diffusion MRI-based AFD complements T2- and FF-mapping techniques to non-invasively assess muscle denervation.

Keywords: Diffusion imaging; fiber diameter; muscle denervation

Submitted Mar 20, 2021. Accepted for publication May 28, 2021.
doi: 10.21037/qims-21-313
View this article at: https://dx.doi.org/10.21037/qims-21-313

Introduction

Peripheral neuropathies may precipitate muscle denervation, whereby loss of innervation at the neuromuscular junction results in muscle weakness. The diagnostic workup of peripheral neuropathies includes a physical exam and frequently, needle electromyography (EMG) to qualify the degree of muscle denervation. Peripheral nerve MRI [MR neurography (MRN)] may be used as an adjunct to directly visualize nerves and muscle. MRN affords the ability to simultaneously evaluate many muscles, included deep-seated ones, which may be difficult to access by EMG. Standard, qualitative MRN uses T_2-weighted, fat suppressed sequences (1) that depict muscle edema during

^ ORCID: 0000-0003-2847-9378.

active denervation (2) and preceding fatty infiltration in the chronically denervated state (3). To better quantify muscle changes, quantitative techniques such as T_2- (4,5) and fat fraction (FF)-mapping (5,6) have been employed to assess the extent of extracellular edema and fatty infiltration, respectively. Quantitative T_2-mapping may also provide superior correlation to EMG as compared to qualitative imaging (7).

Quantitative diffusion-weighted imaging (DWI) may complement T_2- and FF-mapping to assess muscle denervation (4). DWI depicts the microscopic movement of water molecules restricted by impermeable or semi-permeable tissue boundaries. In muscle, diffusion imaging has demonstrated sensitivity to microstructural changes following exercise (8), and in the assessment of primary myopathies (9,10). Monte-Carlo simulations have shown that muscle cell size (or diameter) most strongly influences diffusion anisotropy and mean diffusivity (11). More specifically, decreased muscle diameter results in reduced radial diffusivity and increased fractional anisotropy (FA). Animal (12,13) and human microscopy studies (14) have both demonstrated that muscle denervation leads to decreased muscle diameter and increased diffusion anisotropy (13). However, muscle denervation studies may be either confounded by effects of edema due to transection surgery (4,13,15,16) or biased by increased T_2 when signal-to-noise ratio (SNR) is inadequate (15), motivating investigating muscle DWI and T_2 *in vivo* in humans.

Muscle DWI typically uses lower diffusion-encoding b-values (300–800 s/mm^2) than those used in the brain (≥800 s/mm^2), in part because of the higher mean diffusivity (~1.6 μm^2/ms) and lower anisotropy (~0.1–0.3) in muscle (17). Also, the need for shorter echo times (TE) to sample short T_2 [normal muscle T_2 ~31.7 ms at 3T (18)] incentivizes reducing b-values to shorten TE, while keeping repetition time (TR) >3 seconds (muscle T1 ~1.4 s at 3T). Previous attempts to model muscle diameter with diffusion have utilized multiple diffusion mixing times (17-19) with either cylindrical (19) or random-permeable (20,21) models. While these approaches thoughtfully utilized stimulated-echo diffusion preparation to obtain shorter TEs (<50 ms) and to interrogate longer diffusion time scales (30–1,500 ms) (22), they reported underestimation of muscle diameter versus histology (19-21): ~30–40 *vs.* ~50–70 μm (20) and ~40–55 μm *vs.* ~55–70 μm in another (21). Other human limb muscle histology studies had reported muscle diameters of 53±16 μm (23) and 62.4–72.2 μm (24). Furthermore, histology may be subject to further shrinkage depending on the fixation method (25), which if true, increases the degree of muscle diameter underestimation. Absence of a multi-compartment model and unaccounted contributions from long-range extra-cellular diffusivity in the interconnected endomysium surrounding the muscle fibers have been proposed as reasons for this underestimation (21).

To reduce sensitivity to long-range diffusivity in the endomysium, smaller Δ time intervals could be utilized, which are typical to the more commonly-used spin-echo diffusion preparation. While spin-echo preparation cannot feasibly acquire long Δ time intervals (given spin-echo TE≈2Δ), it provides twice the signal and has shorter scan times than stimulated-echo preparation due to its higher multi-slice-efficiency. Furthermore, improvements to MRI gradient hardware performance have enabled shorter TEs (<60 ms) to be achieved with spin-echo preparation. To incorporate multi-compartment models, the previously proposed cylindrical model (19) could be used. However, the model contains many terms for fitting (intracellular water diffusivity, parallel diffusivity, extracellular water diffusivity in addition to diameter and diffusion orientation), which may require up to 104 diffusion directions (19) encompassing multiple b-values in order to resolve all of these terms adequately. To avoid over-parameterized diffusion fitting that can cause poor convergence and sensitivity to noise, the data dimensionality could be reduced by selecting fewer appropriate parameters to improve fitting accuracy. This could be achieved, for instance, with dictionaries for improving angular fitting (26,27). Additionally, tissue-specific multi-compartment models (28,29) could provide an efficient basis set by utilizing tissue-specific diffusivity values from the literature.

This work proposes a diffusion-based method with tissue-specific, multi-compartment modeling to estimate the skeletal muscle cell (myocyte) diameter, subsequently referred to as the apparent muscle fiber diameter (AFD), using spin-echo diffusion preparation. The primary aim was to assess AFD changes due to muscle atrophy in muscle denervation subjects. It was hypothesized that AFD would be significantly reduced in denervated muscle relative to non-denervated muscle. Quantitative T_2- and FF-maps were also acquired to determine their correlation to diffusion metrics.

Methods

To obtain the AFD, an orientation-invariant dictionary-based approach was proposed (*Figure 1A*). The dictionary

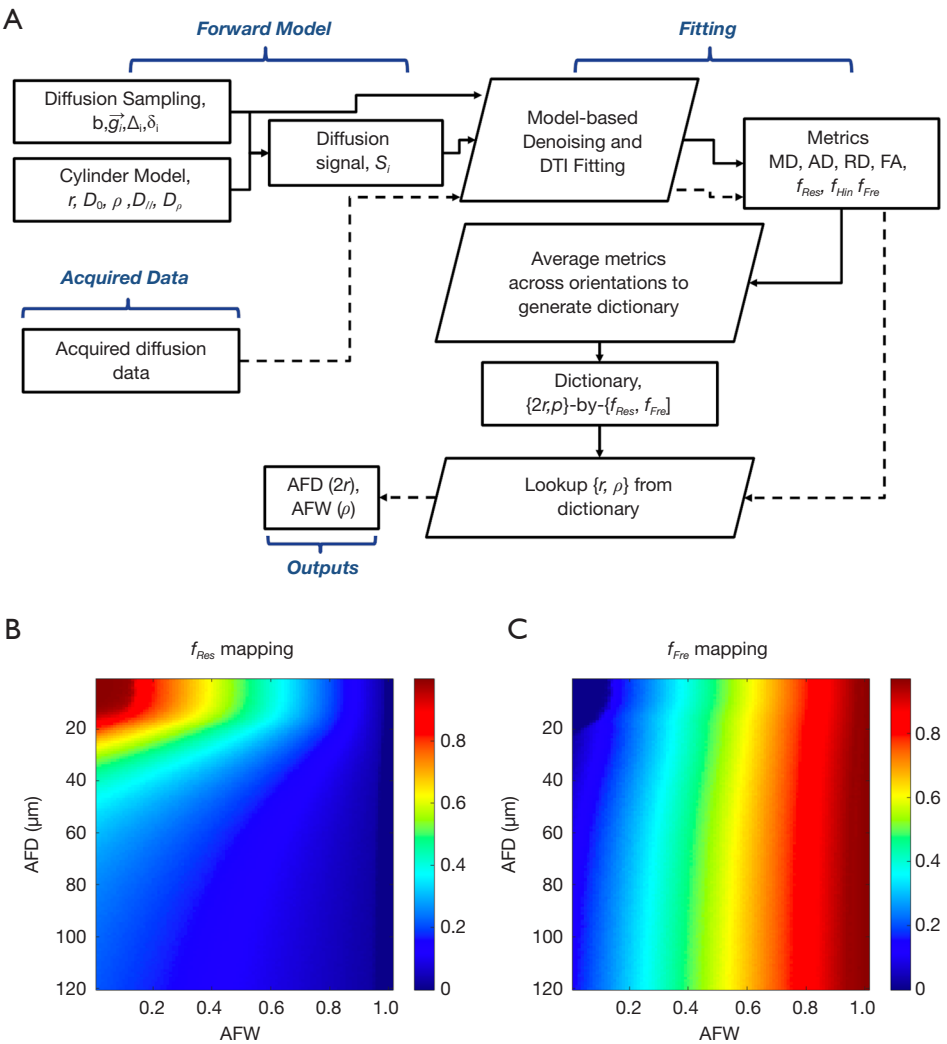

Figure 1 Orientation-invariant dictionary. (A) Flowchart, showing process of dictionary generation beginning with generation of radius (r) and apparent fluid weight (ρ) using a forward model, followed by fitting (solid arrows), followed by fitting the acquired data (dashed arrows), to look up apparent fiber diabeter (AFD or $2r$) and apparent fluid weighting (AFW or ρ) from the dictionary. (B,C) Exemplary maps of restricted (f_{Res}) and free (f_{Fre}) fractions dictionaries with AFD and AFW as inputs.

was generated by first using different simulated muscle fiber diameters and fluid weightings as inputs, and the forward model-generated diffusion signals as outputs. Diffusion signals were then fitted using both a multi-compartment model (28) and the DTI model to obtain diffusion metrics (note: only the multi-compartment model was utilized in the final dictionary for reasons evident in the results). When averaged across a large number of fiber orientations, the diffusion metrics become orientation invariant. The dictionary was formed by the matrices of diffusion metrics *vs.* fiber diameter and fluid weighting (*Figure 1B*). The diffusion metrics resulting from fitting the image data were referenced against the dictionary to infer the AFD and apparent fluid weighting (AFW).

Forward model utilizing a cylinder model

The forward model assumed spins from a combination of muscle and extracellular fluid (blood, synovial fluid, not endomysium) compartments. For the muscle compartment, a well-known, closed-form expression for cylinder-based (19,30,31) radial-diffusivity was used with these parameters:

Table 1 Parameters of the multi-compartment model, forward model parameters and the dictionary

Diffusion Group and its Fraction	Range of mean diffusivity (μm^2/ms), linearly distributed within the range by K intervals	Fractional anisotropy	# of compartments (Diffusivity × Directions, K × N)
Multi-compartment model parameters			
Restricted, f_{Res}	2.1–2.4	0.11–1.00	3×60
Hindered, f_{Hin}	0.6–2.2	0.0	5×1
Free, f_{Fre}	6.0–30.0	0.0	5×1
Noise/Fat, f_{Noise}	0.2–0.4	0.0	2 ×1
Forward model parameters			
Intracellular	Water diffusivity, D_0 (μm^2/ms)	3.3	
	Restricted parallel diffusivity, $D_{//}$	2.1	
	Number of orientations, $N_{orientations}$	30	
Extracellular	Extracellular fluid diffusivity D_F (μm^2/ms)	15.0	
Imaging	Nominal mixing time, Δ (ms)	19.5	
	Nominal pulse width, δ (ms)	11.7	
	Nominal b-values [and directions]	375 [13], 750 [27]	
	SNR	200	
Dictionary parameters			
Apparent fiber diameter, 2r (AFD, μm)		1.0 to 120 (steps of 1.0)	
Apparent fluid weight, ρ (AFW)		0 to 1.0 (steps of 0.01)	

cylinder radius, r, and intrinsic intracellular water diffusivity, D_0. For axial-diffusivity $D_{//}$, Gaussian diffusivity was assumed. The fluid compartment assumed isotropic, Gaussian diffusivity, D_F, for depicting either perfusion or corruption by bulk motion, whereby the fluid weighting was denoted ρ. The AFD is the dictionary-inferred value of 2r, and AFW that of ρ. The diffusivity signal for the i-th acquisition, S_i, could be expressed as a weighted sum of signals arising from the intracellular compartment $S_{M,i}$, the extracellular fluid compartment $S_{F,i}$ and additive noise (Gaussian in complex, Rician distribution in magnitude) η:

$$S_i\left(r,\rho,\vec{g},\delta,\Delta\right)=\left(1-\rho\right)S_{M,i}\left(r,\vec{g},\delta,\Delta\right)+\rho S_{F,i}\left(\vec{g},\delta,\Delta\right)+\eta \quad [1]$$

Signals were generated as a function of diffusion sampling parameters used in the pulse sequence, which included the maximum b-value used, b, the gradient vector $\vec{g}$, the pulse width δ, and the inter-pulse interval Δ. To render orientation invariance between the chosen gradient vector table and the primary muscle fiber axis, the signal of Eq. [1] was computed multiple times ($N_{orientations}$~30), each at different orientations tessellated on a unit sphere. The forward model generation of the dictionary represents a small computational overhead per scan, about 50 seconds (2.8GHz Quad-Core Intel i7, 16GB RAM). The equations for $S_{M,i}$ and fluid $S_{F,i}$ are included in Appendix 1.

Fitting with multi-compartment model

Fitting of the simulated data from the forward model was performed with both DTI and a tissue-specific multi-compartment model (28). DTI provides standard metrics such as mean diffusivity (MD), axial diffusivity (AD), radial diffusivity (RD) and FA. Multi-compartment modeling combines a high degree of freedom for fitting with an efficient basis set for tissue-specific diffusivity values to be used, as applied for brain (28), peripheral nerve (29) and breast (32) anatomies. For skeletal muscle, the multi-compartment model used 192 degrees of freedom (*Table 1*), assumed diffusion signal as a summation of anisotropic (muscle) and isotropic (muscle and extracellular fluid) compartments, and outputs compartment fractions for each assumed diffusivity

value, as detailed in Appendix 2. Four compartment groups were assumed: restricted (f_{Res}, with anisotropic diffusivity approximating muscle), hindered (f_{Hin}, isotropic with mid-range diffusivity approximating generic tissue including muscle), free (f_{Fre}, isotropic with high diffusivity approximating fluid from perfusion, synovium and motion) and noise/fat (f_{Fat}, isotropic and low diffusivity), whereby $f_{Res}+f_{Hin}+f_{Fre}+f_{Fat}=1$. In particular, f_{Res} is analogous to FA, but potentially excludes effects due to perfusion and motion.

Orientation-invariant dictionary

For every set of {r, ρ, orientation} values, every diffusion metric was averaged across fiber orientations a {f_{Res}, f_{Fre}, MD, AD, RD, FA}-by-{r, ρ} orientation-invariant dictionary. The fat and hindered compartments may be excluded from the dictionary (but not from fitting) if fat is negligible and hindered is redundant (fractions sum to one). Diffusion metrics from the actual diffusion acquisition itself are used to lookup {2r=AFD, ρ=AFW} values from the dictionary.

Signal simulations

The values for the compartments (*Table 1*) were chosen to approximate skeletal muscle (restricted) (8,10,11), generic isotropic soft tissue (hindered) and blood flow and synovial fluid (free). For the forward model, intracellular diffusivity D_0, was set to approximate water diffusivity at human body temperature (33), while axial diffusivity $D_{//}$ was set to approximate values in the literature (17). The range of values for 2r (10 to 120 μm) considered literature values (21,23,24) of muscle diameter. A 120-by-100 {r, ρ} dictionary was generated.

Simulation goals were to evaluate (I) how metrics varied with r, SNR, ρ, D_0 and $D_{//}$, and (II) which metrics were sufficient to obtain AFD=2r while providing the lowest bias and precision errors. The values of 2r evaluated were from 15 to 110 μm to stay within the dictionary values (10 to 120 μm). The impact from variation in the following parameters were also evaluated: SNR (varied from 15–1,000), ρ (0–0.15), $D_{//}$ (1.9–2.5 μm^2/ms) and D_0 (2.7–3.6 μm^2/ms). Each parameter was simulated at four intervals. Each simulation involved 30 noise instances. To allow different diffusion metrics to be compared, precision error ε and bias error β as derived in Appendix 3 were computed in units of r (μm).

Human subjects imaging protocol

The study was conducted in accordance with the Declaration of Helsinki (as revised in 2013). Under an IRB-approved protocol (IRB 2015-441), we prospectively recruited and obtained written consent from 16 patients (age =44.5±16.6 years, 7 female, 9 male) undergoing standard-of-care MRN with suspected denervation of shoulder girdle muscles based on electrodiagnostic findings and qualitative real-time MRI assessment. A total of 18 patient exams were included (2 with bilateral denervation). Bilateral shoulder MRI (n=8 total exams) was acquired in 4 healthy volunteers (age =25.6±1.3 years, 1 female, 3 male), to serve as unmatched controls. ROIs were placed manually within six separate muscles (supraspinatus, infraspinatus, subscapularis, and deltoid anterior/middle/posterior heads) on 3 or more images (of area 1.16±0.98 cm^2) from a 3D gradient-echo acquisition, avoiding inclusion of tendon slips or the peripheral investing fascia.

Muscles were categorized into three groups – control (healthy volunteers), non-denervated (patients) and denervated (patients). Denervation was determined by one board-certifed radiologist by the presence of diffusely increased muscle signal intensity ('edema pattern') on 2D T_2-weighted Dixon-FSE water (fluid-sensitive) images, acquired as part of the standard-of-care MRN protocol. Excluding muscle ROIs with EPI artifacts or specific muscles not captured within the FOV, there were a total of 47 control (8 control exams × 6 ROIs minus one outside FOV), 36 non-denervated, and 68 denervated (18 exams × 6 ROIs minus four with artifacts) muscles evaluated. EMG results were available for 15 of the 18 patient scans (52/68 denervated muscles) and these confirmed the presence or absence of muscle denervation. Control subjects were confirmed to not have muscle edema patterns on MRI, upon radiologic review.

MRI was performed at 3T field strength (Signa Premier, GE Healthcare, Chicago, IL, USA) with oblique-axial, multi-b-valued DTI with FOV =27 cm, TR/TE/ESP =3,300/56/0.6 ms, b-value =0 s/mm^2 (2 directions), 375 s/mm^2 (13 directions) and 750 s/mm^2 (27 directions), 3 mm-isotropic resolution, 35–38 slices, and 5 minutes total scan time. Two shots with multiplexed sensitivity encoding (MUSE) reconstruction, and parallel imaging factor =1.5 were used to reduce effects of image distortion. Two, 16-channel flexible receiver coil arrays (Neocoil, Pewaukee, WI, USA) were used. The diffusion pulses used gradient amplitudes of 6.68–6.70 G/cm, Δ=19.5–22.7 ms, and δ=11.1–11.9 ms, and were stored on the DICOM header to generate scan-specific dictionaries.

For comparison against diffusion metrics, 2D FSE T_2-

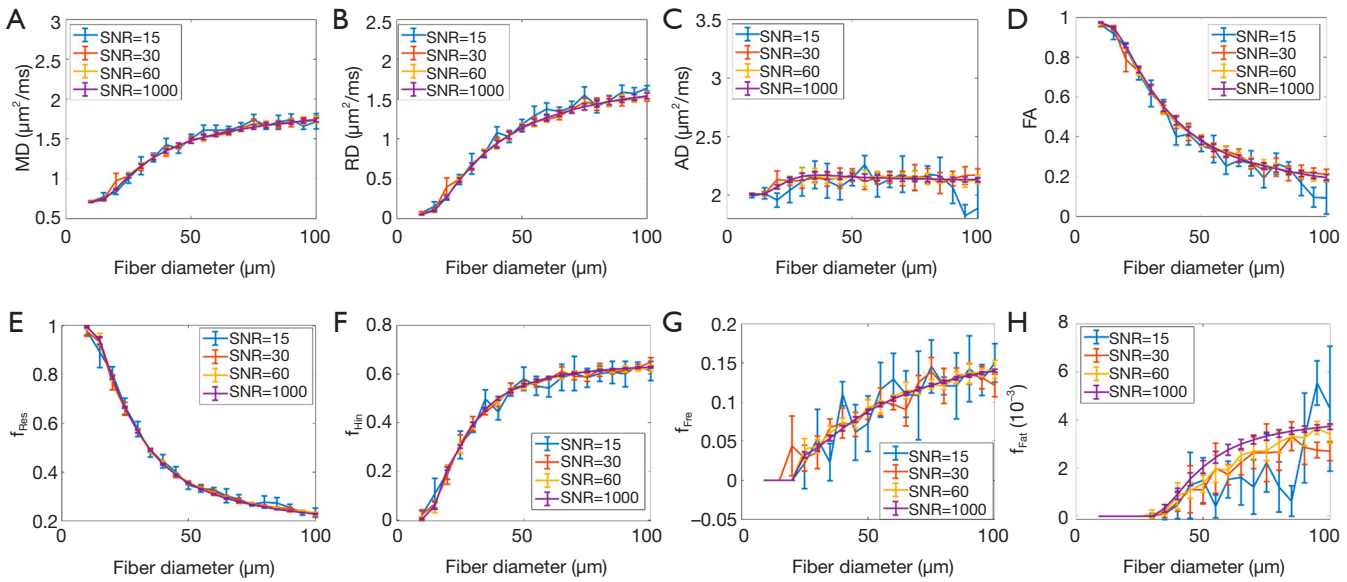

Figure 2 Simulation results of diffusion metrics obtained at different simulated fiber diameters and signal-to-noise (SNR) levels, for mean diffusivity (A), radial diffusivity (B), axial diffusivity (C), fractional anisotropy (D), and compartment fractions for restricted diffusion (E), hindered diffusion (F), free diffusivity (G) and fat/noise (H).

mapping was performed with eight echoes and an echo spacing of 11 ms, along with B_{1+} mapping using the Bloch-Siegert method (34). For FF-mapping, 3D two-point Dixon gradient echo was used. Total scan time for the quantitative sequences (diffusion, T_2, B_{1+} and FF-mapping) was under 10 minutes.

Processing of quantitative images

The diffusion images were corrected for gradient nonlinearity bias (35) to obtain MD, RD, AD, FA, f_{Res}, f_{Hin}, f_{Fre}, f_{Fat}, AFD and AFW; this was essential due to the typically large offset of the shoulder muscles with respect to magnet isocenter. T_2-maps were processed with B_{1+} correction (36), while fat fraction (FF) and T_2-maps were adjusted for relaxation (37), assuming nominal values of muscle at 3T (T_1=1,420 ms, T_2=38 ms). Non-rigid image registration (38) was used to align both T_2-mapping magnitude and diffusion b=0 images to the 3D gradient-echo water image for analysis (Elastix, RRID:SCR_009619).

Statistical analysis

A two-sample *t*-test (type I error, α=0.05) was used to compare each metric among the three groups: control, non-denervated and denervated muscles (R, The R Foundation). Holm-Bonferroni correction was applied for multiple comparison. Comparisons were also made for each muscle region using Wilcoxon rank sum test, if at least 6 datapoints were available.

Pearson correlation between the key metrics of AFD, FA, T_2 and FF was also performed to determine associations. Correlation (anti-correlation) between 0 to 0.29 (0 to −0.29) was deemed negligible, 0.30 to 0.49 (−0.30 to −0.49) low, 0.50 to 0.69 (−0.50 to −0.69) moderate, 0.70 to 0.89 (−0.70 to −0.89) high, and 0.90 to 1.00 (−0.90 to −1.00) very high.

Results

Simulations

Figure 2 shows increasing the simulated diameter increased MD (*Figure 2A*), RD (*Figure 2B*), f_{Hin} (*Figure 2F*), and f_{Fre} (*Figure 2G*), but decreased FA (*Figure 2D*) and f_{Res} (*Figure 2E*). AD (*Figure 2C*) was constant with diameter. Changes to f_{Fat} (*Figure 2H*) were negligible (~0.4% effect). Reducing SNR increased errors (*Figure 2A-H*). For every SNR level tested, the best precision was found in f_{Res}, with $\varepsilon(f_{Res})$=0.45-1.54 μm (as evident in *Figure 2E*). Bias resulting from varying SNR was also lowest in f_{Res} [$\varepsilon(f_{Res,SNR})$=0.36 μm], depicted by the close trendlines in *Figure 2E*.

Figure 3 shows increasing ρ increased MD (*Figure 3A*),

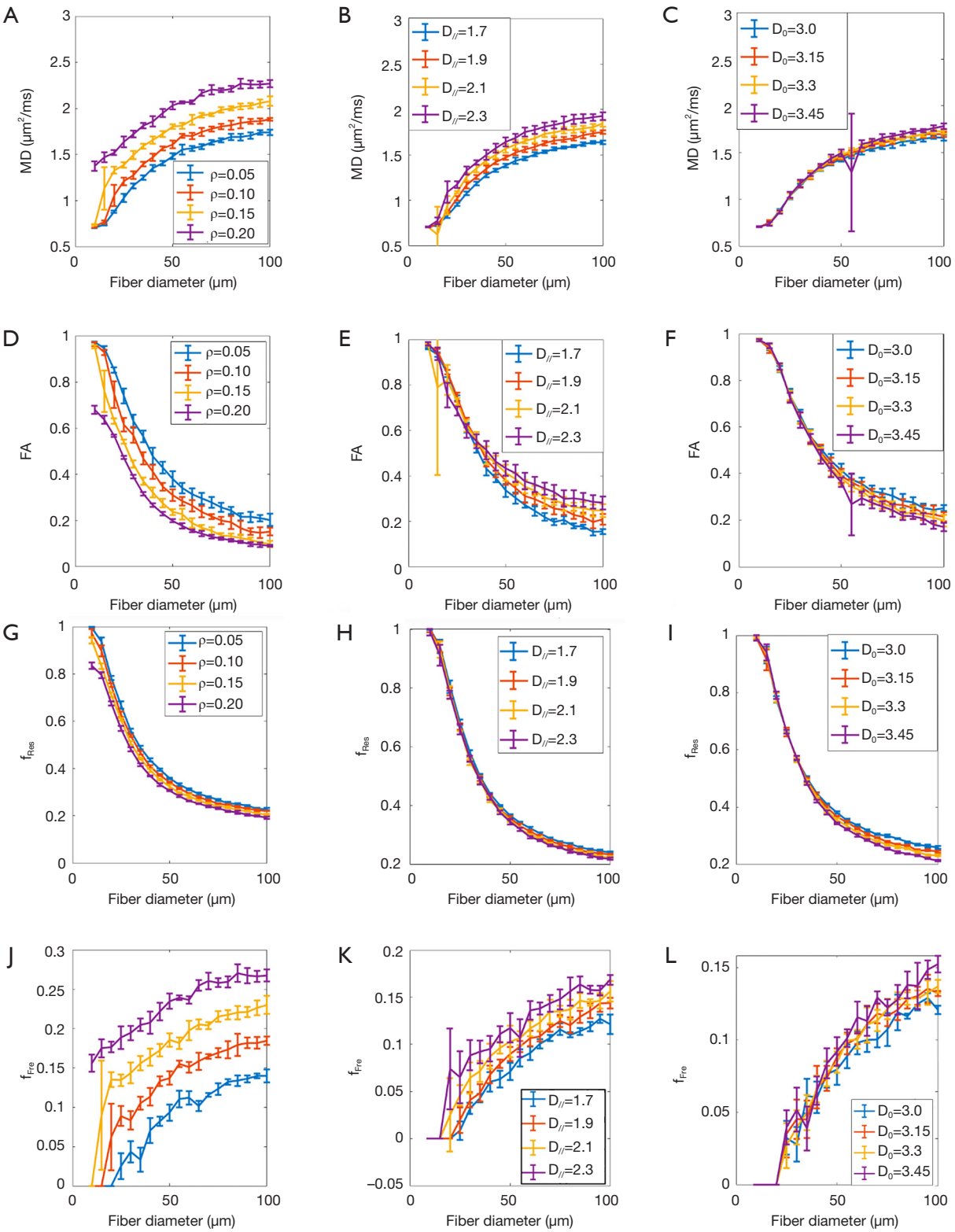

Figure 3 Simulation results of mean diffusivity (A-C), fractional anisotropy (D-F), restricted fraction (G-I) and free fraction (J-L) under different apparent fluid weight (left column), parallel diffusivity (middle column), and intracellular water diffusivity (right column).

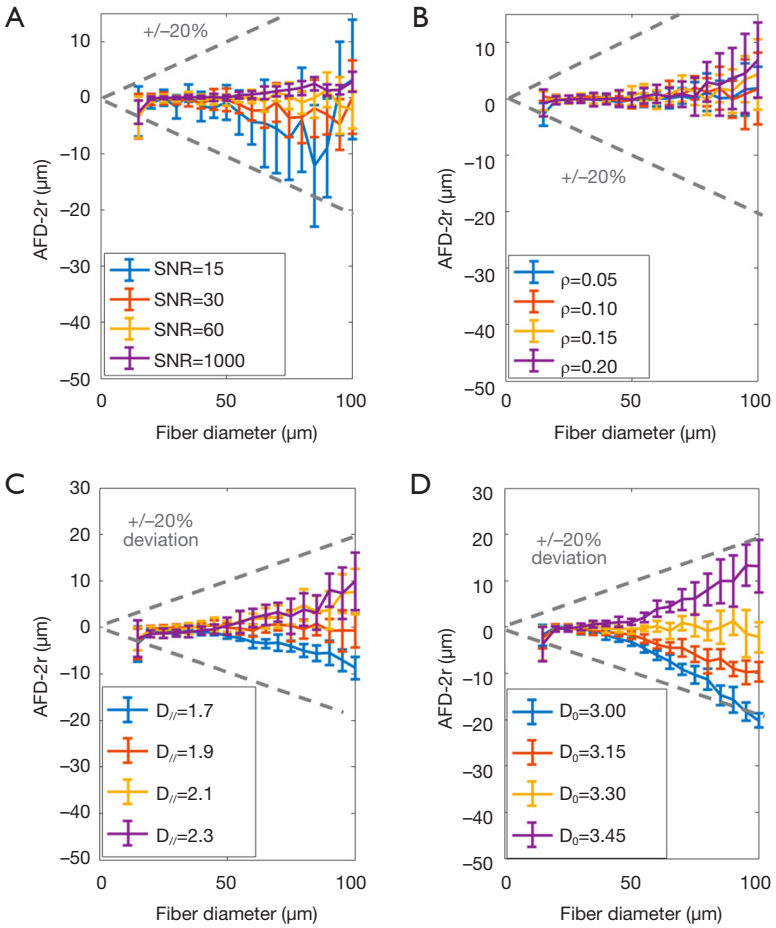

Figure 4 Bland-Altman plots of apparent fiber diameter (AFD) under simulated variation of signal-to-noise ratio (SNR) (A), ρ (B), parallel diffusivity (C), and intracellular water diffusivity (D), with ±20% deviation dashed lines indicated. While most plots were within 20%, at the smallest diameter of 10 μm, mean errors below –20% (–3.6 to –9.9 μm) were observed.

but decreased FA (*Figure 3D*). Increasing $D_{//}$ increased MD (*Figure 3B*) across all diameters and FA (*Figure 3E*) at larger diameters. Increasing D_0 increased MD (*Figure 3C*) across all diameters but decreased FA (*Figure 3F*) at larger diameters. The trendlines for f_{Res} were similar to that of FA, but were more closely distributed. The biases and precision errors in f_{Res} were lower than in FA [$\beta(f_{Res})$=0.36–1.89 μm *vs.* β_{FA}=1.36–5.18 μm, $\varepsilon(f_{Res})$=0.44–0.68 μm *vs.* ε_{FA}=0.65–3.06 μm]. For every set of simulated parameters, bias and precision were the best in f_{Res}. *Figure 3J,3K* show the plots for f_{Fre}, which increased slightly with increased AFW, $D_{//}$ and D_0. The trend in f_{Fre} appeared to be complementary to f_{Res}.

Figure 4 shows Bland-Altman plots of radial AFD error versus simulated 2*r* (AFD-2*r*), with AFD obtained with a dictionary using only f_{Res} and f_{Fre}. Reduced SNR and reduced D_0 resulted in lower AFD. $D_{//}$ and ρ changes did not alter AFD significantly. All mean errors were within ±20% deviation.

In vivo comparisons between muscle groups

The mean AFD in controls was 89.7 μm, non-denervated was 71.2 μm, and denervated was 60.7 μm (*Table 2*). Significant differences in AFD (denervated < non-denervated < controls), FA (denervated > non-denervated > controls), T_2 (denervated > non-denervated > controls), FF (denervated > non-denervated, and deneverated > controls) and RD (denervated < controls) were observed.

For comparisons by muscle regions (e.g., supraspinatus, infraspinatus, etc.), 6 muscles could be compared between controls and denervated, but only 3 muscles could be compared between non-denervated and controls/denervated

Table 2 Summary of *in vivo* results comparing healthy controls *vs.* non-denervated patients (Non-den.) *vs.* denervated patient muscles (Den.), with mean and P values from two-sample *t*-tests (α=0.05, statistical significance with Holm-Bonferroni correction for multiple comparison indicated by *), and number of statistically-significantly different muscle regions of interests (ROIs)

Metrics	Mean (Standard Deviation) Values			P values			Number of statistically-significant different muscle ROI comparisons		
	Controls	Non-den.	Den.	Controls *vs.* Non-den.	Non-den. *vs.* Den.	Controls *vs.* Den.	Controls *vs.* Non-den.	Non-den. *vs.* Den.	Controls *vs.* Den.
MD (μm^2/ms)	1.782 (0.119)	1.802 (0.234)	1.739 (0.217)	0.639	0.171	0.177	0/3	0/3	0/6
FA	0.148 (0.045)	0.173 (0.051)	0.219 (0.056)	0.021*	<0.001*	<0.001*	0/3	0/3	3/6
AD (μm^2/ms)	2.073 (0.106)	2.133 (0.200)	2.143 (0.192)	0.092	0.802	0.017	0/3	0/3	0/6
RD (μm^2/ms)	1.637 (0.146)	1.636 (0.262)	1.536 (0.243)	0.979	0.055	0.008*	1/3	0/3	0/6
AFD (μm)	89.68 (13.59)	71.57 (15.32)	60.69 (15.91)	<0.001*	0.001	<0.001*	2/3	2/3	6/6
AFW (%)	8.18 (3.90)	9.64 (8.18)	10.32 (6.45)	0.302	0.653	0.033	0/3	0/3	1/6
T2 (ms)	35.51 (1.65)	38.65 (3.53)	54.01 (15.31)	<0.001*	<0.001*	<0.001*	2/3	3/3	6/6
FF (%)	3.408 (1.018)	3.343 (1.083)	8.427 (10.852)	0.772	<0.001*	<0.001*	2/3	1/3	1/6

each (*Table 2*). This yielded 12 total comparisons per metric. Statistically-significant differences were noted for AFD (10/12), FA (3/12), T_2 (11/12), FF (4/12) and RD (1/12).

Figure 5 demonstrates how quantitative differences could be observed in the denervated muscles relative to surrounding non-denervated muscles on FA, AFD and T_2-maps. MD, RD and AD did not provide contrast between non-denervated and denervated muscles.

Figure 6 shows higher AFD maps in muscles of healthy control (*Figure 6C*,*6D*), relative to those from a patient with idiopathic neuropathy causing severe muscle weakness (*Figure 6G*,*6H*).

Correlation between quantitative maps in vivo

Low correlation between AFD and FA was observed (–0.450, P<0.001) (*Figure 7A*). Moderate correlation was observed between FF and T_2 (0.544, P<0.001) (*Figure 7B*), but the linear trend appeared to deviate into two at high T_2 (>45 ms): one with high FF (>20%), and the other with low FF. Low correlation between FA and T_2 (0.365, P<0.001) was observed (*Figure 7C*), while correlation between FA and FF was negligible (0.184, P=0.024) (*Figure 7D*). Moderate correlation between AFD and T_2 (–0.532, P<0.001) was observed (*Figure 7E*). There was a cluster of very high T_2 (>80 ms) datapoints with smaller FA (0.17–0.22) and larger AFD (55–105 μm), which deviated from the linear fit. Low correlation was observed between AFD and FF (–0.395, P<0.001) (*Figure 7F*); a cluster of datapoints with high FF (>20%) were observed to have mid-range FA but low AFD.

Discussion

This work proposes a new apparent fiber diameter (AFD) metric, obtained by an orientation-invariant dictionary modeling muscle fibers as cylinders with radial, restricted diffusivity. Significant AFD differences between denervated, non-denervated and normal control muscles were observed. Simulations suggest that lower AFD in denervated muscle could be explained by either a true reduction in muscle diameter, reduced intracellular diffusivity, or lower SNR. The latter two reasons could be ruled out. Increased, rather than decreased, intracellular diffusivity (D_0) would be expected in muscle denervation due to the breakdown of myofibrillar proteins. As such, it was unlikely that decreased D_0 caused lower AFD in denervated muscle. The SNR was also unlikely to be lower in patients, because T_2 (and hence SNR) was likely higher in denervated muscle. We have anecdotally measured mean SNR between 46–196 in two of the patient subjects, which was just under our targeted SNR of 200 but was within range of the simulated SNRs. While reduced AFD (by 18.1 μm) and increased T_2 (by 3.1 ms) between normal muscles in controls and non-denervated muscles in patients were unexpected, these could be due to differences in age, cumulative effects of protein breakdown due to disuse [0.5–0.6% per day (39)] or alternatively,

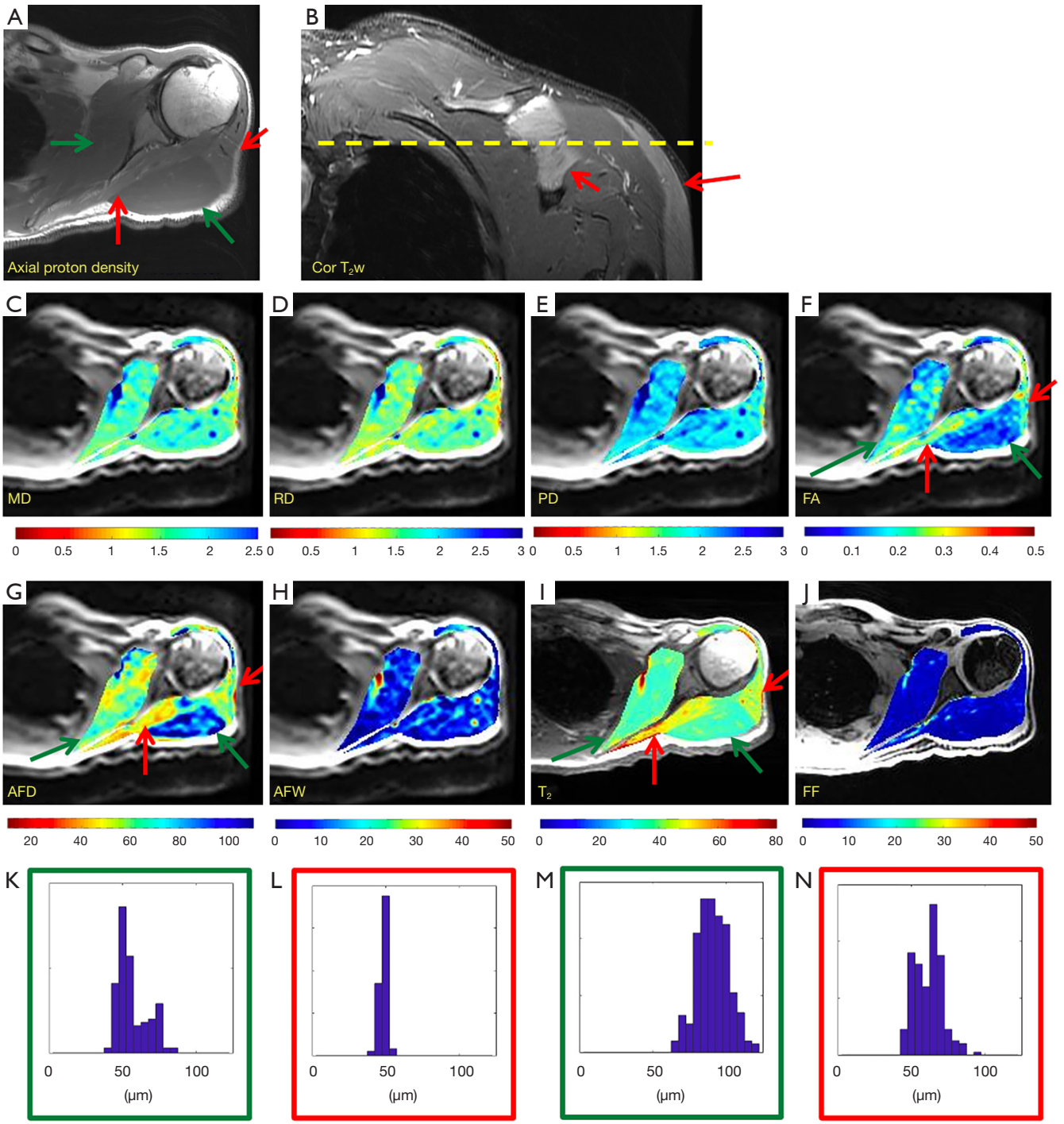

Figure 5 Quantitative maps from a 47-year-old male with muscle edema patterns observed in the left infraspinatus, and middle deltoid muscles. (A) Qualitative proton density axial image corresponding to slice position in yellow-dashed line of (B) coronal T_2-weighted Dixon water image, and (C-J) quantitative maps. The mean diffusivity (MD), radial diffusivity (RD) and axial diffusivity (AD) maps (in $\mu m^2/ms$) do not provide contrast in denervated muscles (red arrows) *vs.* non-denervated muscles (green arrows), but fractional anisotropy (FA), apparent fiber diameter (AFD) (μm) and T_2-maps (ms) do. No fatty infiltration was observed in the fat fraction (FF) (%) maps. Most pixels in the apparent fluid weighting (AFW) (%) were mostly low (<20%). AFD histograms show higher AFD in (K) non-denervated subscapularis *vs.* (L) denervated infraspinatus, and (M) non-denervated posterior deltoid *vs.* (N) denervated middle deltoid.

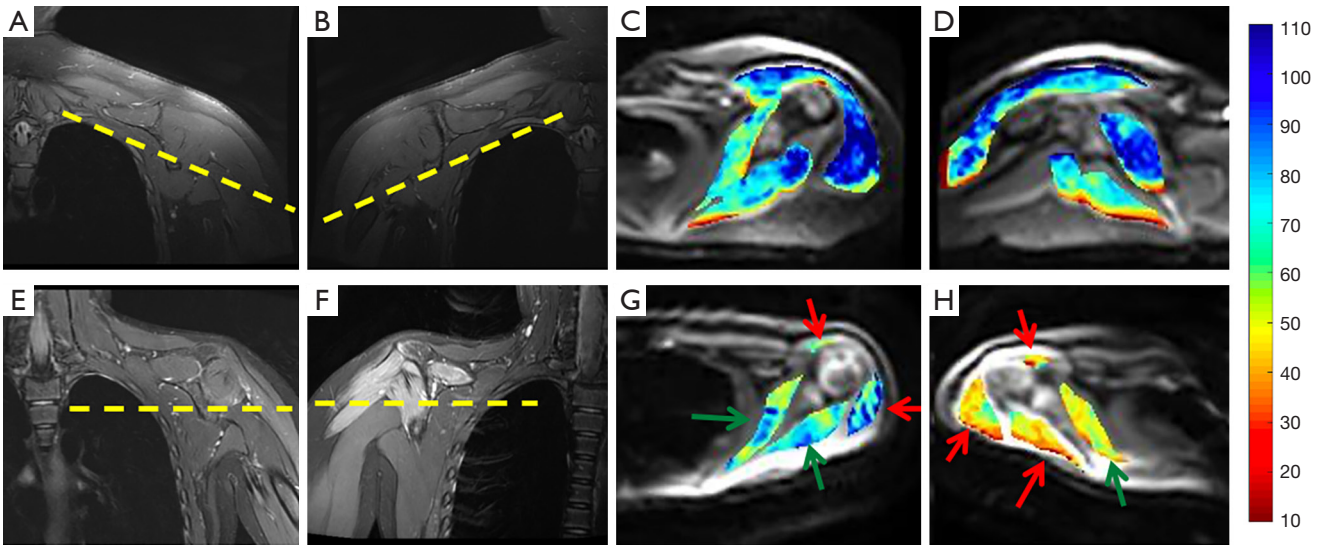

Figure 6 Apparent fiber diameter (AFD) maps (in μm) from bilateral exams of two subjects. (A-D) A healthy subject (25-year-old female) with no muscle edema patterns, with coronal T2-weighted Dixon water images (A,B) and corresponding slice position (dashed yellow lines) of quantitative maps, showing high AFD in the left (C) and right (D) shoulder muscles. (E-H) An 11-year-old female imaged bilaterally with the clinical suspicion of Parsonage-Turner syndrome (an idiopathic neuropathy causing severe muscle weakness); coronal T_2-weighted Dixon and corresponding slice position of quantitative maps in dashed yellow lines (E,F). Clinical exam reported deltoid weakness on the left (G) and right (H), and infraspinatus and supraspinatus (not shown) weakness only on the right. The weaker right deltoid and infraspinatus muscles (2/5 British Medical Research Council muscle grade testing) than the left (3/5) was consistent with lower AFD on the right (H) than the left (G). Red arrows point to denervated muscle identified on MRI, green arrows to non-denervated muscle.

overuse due to compensation. As compared to FA, AFD was shown in simulations, *in vivo* comparisons by muscle-ROI, and in correlations with T_2 and FF to better depict muscle atrophy. A negative correlation of AFD with T_2 agrees with either increased extracellular space in denervated muscle (14) or protein loss (40) concomitant with muscle atrophy.

Despite the small sample size (n=16), the measured AFD range of 71–119 μm in shoulder muscles of healthy controls in our study compared well with literature values from human limb muscle histology [mean 53±16 μm, range 8–109 μm (23), and mean values between 62.4–72.2 μm (24)]. In comparison, previous work using stimulated-echo diffusion preparation and longer mixing times (30–1,500 ms) underestimated muscle diameters [~30–40 μm in (20); ~40–55 μm in (21)]. We speculate that the larger AFD values obtained in our study could be attributed to one or more factors: (I) using multiple b values with fixed Δ intervals along with spin-echo preparation; (II) assuming constant D_0 and $D_{//}$ to reduce fitting dimensionality, which was not done previously (19); and (III) contribution from the extracellular endomysium due to semi-permeable membranes.

While Monte-Carlo simulations reveal correlations between DTI-based FA and muscle diameter and permeability (11), previous animal studies have not conclusively demonstrated FA increases secondary to muscle denervation (13,15,16). In comparison, results of the current study suggest that *in vivo* AFD mapping in humans may provide a more robust depiction of intracellular muscle microstructure changes compared to FA. In addition, deviations from linear fitting of both AFD versus T_2 and FA versus T_2 were noted in datapoints with high T_2 (>80 ms), which suggests that diffusivity changes with T_2 may be biphasic. Mechanisms for T_2 increases in denervation include increased extracellular space (14), intracellular fluid increases (due to exercise) (41) and loss of myofibrillar proteins (42) leading to changes in membrane permeability. In such scenarios, it is conceivable that diffusion anisotropy might decrease and AFD might increase as suggested by previously reported simulations (11). Investigating permeability could be incorporated in future studies utilizing spin-echo-prepared diffusion sampling schemes with multi-Δ acquisition (43).

While this work focused on the AFD metric, AFW (apparent fluid weighting) could potentially be another biomarker of interest. Anecdotally, patterns of high AFW were

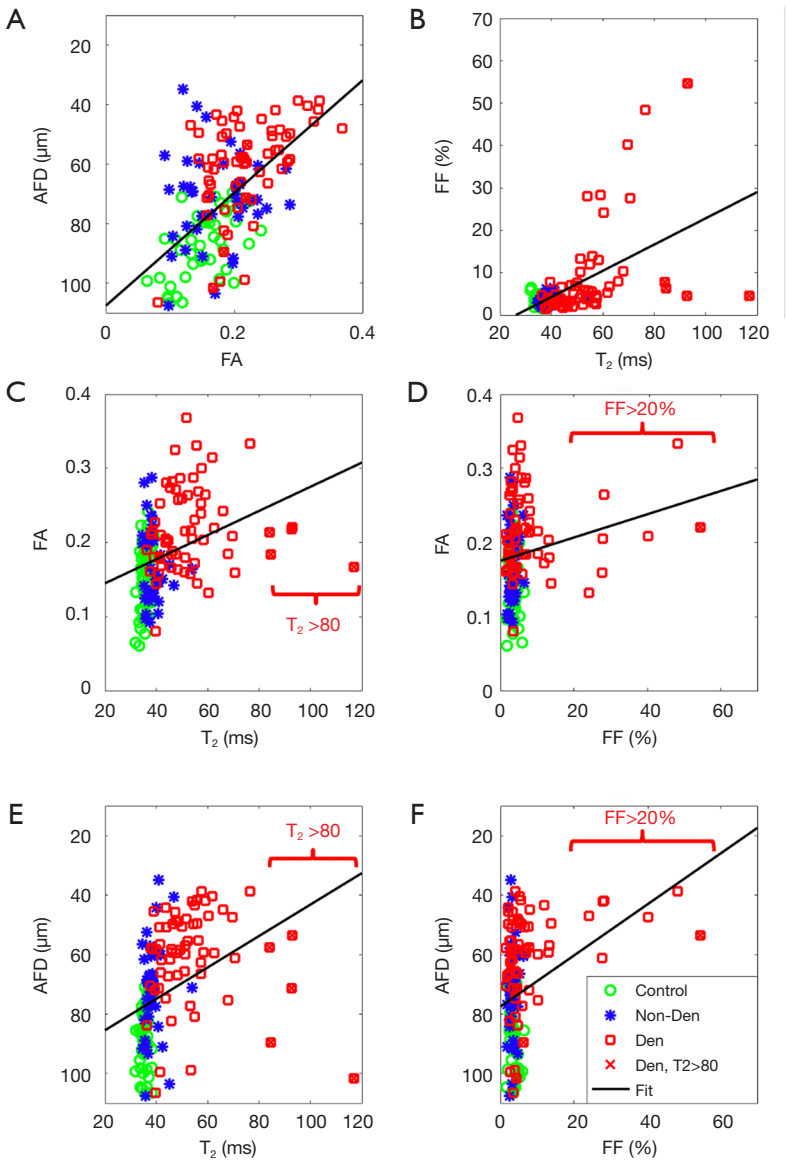

Figure 7 Scatter plots between apparent fiber diameter (AFD), fractional anisotropy (FA), T_2 and fat fraction (FF), showing (A) moderate correlation between AFD and FA (–0.582, P<0.001), (B) moderate correlation between FF and T_2 (0.544, P<0.001) with two trends that diverge from the linear fit, (C) low correlation between FA and T_2 (0.359, P<0.001), (D) low correlation between AFD and T_2 (–0.358, P<0.001), (E) negligible correlation between FA and FF (0.197, P=0.016), and (F) low correlation between AFD and FF (–0.331, P<0.001). The FA and AFD data points with high T_2>80 ms appeared to diverge from the main trends in (C,D). High FF (>20%) data points deviated from the trendline in the FF-FA plot (F).

observed to correspond to perfusion from blood vessels, as did maps of f_{Fre} within this study and in another study using the multi-compartment model (32); however, these relationships were not analyzed in this work. Fluid-like, high diffusivity values could also be caused by bulk motion that contribute to second-order moments. For a b value of 750 s/mm^2 and Δ ~20 ms, diffusion gradients would be sensitive to bulk motion velocity changes of ~0.4 mm/s. The chest wall and shoulder regions are potentially susceptible to respiratory motion and involuntary shoulder motion. These motion effects could be mitigated by respiratory-gating (44) and possibly by reduced scan time.

Prior experiments suggest that transverse diffusivity (i.e., λ_2 and λ_3 values) differences from the DTI model can depict muscle fiber ellipticity (45). In the current work, the model-based denoising assumed no ellipticity ($\lambda_2=\lambda_3$). However, the susceptibility of the smallest eigenvalue (λ_3) to noise and added model complexity, accounting for both major- and minor-axes' diameters, could impede modelling ellipticity.

Limitations and future work

This preliminary work was limited by the low number of patient subjects (n=16, 18 exams), possible bias due to lack of age- and sex-matched in the healthy control cohort, and lack of EMG confirmation of muscle denervation in three of the patient subjects. Future studies would include larger patient cohorts and correlating quantitative AFD against EMG results.

Validation of AFD was also not performed against a ground truth, such as histological microscopy of *ex vivo* muscle specimens. Potential issues with validation could include tissue dehydration and translability of non-human specimens to clinical imaging results. As next steps, we plan to validate the AFD results and methods against histology by performing *in vivo* diffusion imaging in human subjects.

The addition of non-invasive muscle diameter measurements to T_2 and FF metrics can provide complementary information to assess muscle denervation. Future work can explore combined analysis of AFD with T_2 and FF measurements. For muscle diameter values to be meaningful on a per-subject basis, baseline measurements may be necessary. Longitudinal, quantitative MRI in patients with muscle denervation may provide added characterization complementary to electrodiagnostics and clinical examination. Diffusion-based muscle diameter measurements may also be applicable in the peripheral musculature of the arms and legs, as well as in other disease processes such as Duchenne muscular dystrophy (10) and diabetic polyneuropathy (46) where standard DTI has been applied.

Conclusions

Diffusion MRI-based AFD complements T_2- and FF-mapping techniques to non-invasively assess muscle denervation.

Acknowledgments

The authors will also like to acknowledge technical assistance from Sophie Queler, Kenneth Serrano, Jaemin Shin and Maggie Fung.

Funding: This work was supported in part by NIH R21-TR003033. The opinions or assertions contained herein are the private views of the authors and are not to be construed as official or reflecting the views of the NIH. The authors also acknowledge research support from GE Healthcare.

Footnote

Conflicts of Interest: All authors have completed the ICMJE uniform disclosure form (available at https://dx.doi.org/10.21037/qims-21-313). ETT and DBS are co-inventors on US Provisional Patent 63/125,887. ETT and DBS receive institutional research support from GE Healthcare.

Ethical Statement: The authors are accountable for all aspects of the work in ensuring that questions related to the accuracy or integrity of any part of the work are appropriately investigated and resolved. The trial was conducted in accordance with the Declaration of Helsinki (as revised in 2013). The study was approved by institutional review board of the Hospital for Special Surgery (IRB 2015-441) and written informed consent was obtained from all individual participants. Patient anonymity has been preserved in this manuscript.

References

1. Tepeli B, Karata M, Cokun M, Yemiçi OÜ. A Comparison of Magnetic Resonance Imaging and Electroneuromyography for Denervated Muscle Diagnosis. J Clin Neurophysiol 2017;34:248-53.
2. Eichelberger L, Akeson WH, Roma M. Effects of Denervation on the Histochemical Characterization of Skeletal Muscle During Growth. Am J Physiol 1956;185:287-98.

3. Kamath S, Venkatanarasimha N, Walsh MA, Hughes PM. MRI appearance of muscle denervation. Skeletal Radiol 2008;37:397-404.
4. Ha DH, Choi S, Kang E, Park HT. Diffusion tensor imaging and T2 mapping in early denervated skeletal muscle in rats. J Magn Reson Imaging 2015;42:617-23.
5. Sinclair CD, Morrow JM, Janiczek RL, Evans MR, Rawah E, Shah S, Hanna MG, Reilly MM, Yousry TA, Thornton JS. Stability and sensitivity of water T2 obtained with IDEAL-CPMG in healthy and fat-infiltrated skeletal muscle. NMR dBiomed 2016;29:1800-12.
6. Janiczek RL, Gambarota G, Sinclair CD, Yousry TA, Thornton JS, Golay X, Newbould RD. Simultaneous T_2 and lipid quantitation using IDEAL-CPMG. Magn Reson Med 2011;66:1293-302.
7. Argentieri EC, Tan ET, Whang JS, Queler SC, Feinberg JH, Lin B, Sneag DB. Quantitative T2 -mapping magnetic resonance imaging for assessment of muscle motor unit recruitment patterns. Muscle Nerve 2021;63:703-9.
8. Hooijmans MT, Monte JRC, Froeling M, van den Berg-Faay S, Aengevaeren VL, Hemke R, Smithuis FF, Eijsvogels TMH, Bakermans AJ, Maas M, Nederveen AJ, Strijkers GJ. Quantitative MRI Reveals Microstructural Changes in the Upper Leg Muscles After Running a Marathon. J Magn Reson Imaging 2020;52:407-17.
9. Sigmund EE, Sui D, Ukpebor O, Baete S, Fieremans E, Babb JS, Mechlin M, Liu K, Kwon J, McGorty K, Hodnett PA, Bencardino J. Stimulated echo diffusion tensor imaging and SPAIR T2-weighted imaging in chronic exertional compartment syndrome of the lower leg muscles. J Magn Reson Imaging 2013;38:1073-82.
10. Hooijmans MT, Damon BM, Froeling M, Versluis MJ, Burakiewicz J, Verschuuren JJ, Niks EH, Webb AG, Kan HE. Evaluation of skeletal muscle DTI in patients with duchenne muscular dystrophy. NMR Biomed 2015;28:1589-97.
11. Berry DB, Regner B, Galinsky V, Ward SR, Frank LR. Relationships between tissue microstructure and the diffusion tensor in simulated skeletal muscle. Magn Reson Med 2018;80:317-29.
12. Saotome T, Sekino M, Eto F, Ueno S. Evaluation of diffusional anisotropy and microscopic structure in skeletal muscles using magnetic resonance. Magn Reson Imaging 2006;24:19-25.
13. Zhang J, Zhang G, Morrison B, Mori S, Sheikh KA. Magnetic resonance imaging of mouse skeletal muscle to measure denervation atrophy. Exp Neurol 2008;212:448-57.
14. Polak JF, Jolesz FA, Adams DF. Magnetic Resonance Imaging of Skeletal Muscle Prolongation of T1 and T2 Subsequent to Denervation. Invest Radiol 1988;23:365-9.
15. Holl N, Echaniz-Laguna A, Bierry G, Mohr M, Loeffler JP, Moser T, Dietemann JL, Kremer S. Diffusion-weighted MRI of denervated muscle: a clinical and experimental study. Skeletal Radiol 2008;37:1111-7.
16. Yamabe E, Nakamura T, Oshio K, Kikuchi Y, Toyama Y, Ikegami H. Line scan diffusion spectrum of the denervated rat skeletal muscle. J Magn Reson Imaging. 2007;26:1585-9.
17. Oudeman J, Nederveen AJ, Strijkers GJ, Maas M, Luijten PR, Froeling M. Techniques and applications of skeletal muscle diffusion tensor imaging: A review. J Magn Reson Imaging 2016;43:773-88.
18. Gold GE, Han E, Stainsby J, Wright G, Brittain J, Beaulieu C. Musculoskeletal MRI at 3.0 T: Relaxation Times and Image Contrast. AJR Am J Roentgenol 2004;183:343-51.
19. Kim S, Chi-Fishman G, Barnett AS, Pierpaoli C. Dependence on diffusion time of apparent diffusion tensor of ex vivo calf tongue and heart. Magn Reson Med 2005;54:1387-96.
20. Fieremans E, Lemberskiy G, Veraart J, Sigmund EE, Gyftopoulos S, Novikov DS. In vivo measurement of membrane permeability and myofiber size in human muscle using time-dependent diffusion tensor imaging and the random permeable barrier model. NMR Biomed 2017;30:e3612.
21. Sigmund EE, Novikov DS, Sui D, Ukpebor O, Baete S, Babb JS, Liu K, Feiweier T, Kwon J, McGorty K, Bencardino J, Fieremans E. Time-dependent diffusion in skeletal muscle with the random permeable barrier model (RPBM): application to normal controls and chronic exertional compartment syndrome patients. NMR Biomed 2014;27:519-28.
22. Karampinos DC, Banerjee S, King KF, Link TM, Majumdar S. Considerations in high-resolution skeletal muscle diffusion tensor imaging using single-shot echo planar imaging with stimulated-echo preparation and sensitivity encoding. NMR Biomed 2012;25:766-78.
23. Maier F, Bornemann A. Comparison of the muscle fiber diameter and satellite cell frequency in human muscle biopsies. Muscle Nerve 1999;22:578-83.
24. Meznaric M, Cvetko E. Size and Proportions of Slow-Twitch and Fast-Twitch Muscle Fibers in Human Costal Diaphragm. Biomed Res Int 2016;2016:5946520.
25. Firshman AM, Valberg SJ, Bender JB, Annandale EJ, Hayden DW. Comparison of Histopathologic Criteria and

Skeletal Muscle Fixation Techniques for the Diagnosis of Polysaccharide Storage Myopathy in Horses. Vet Pathol 2006;43:257-69.
26. Daducci A, Canales-Rodriguez EJ, Descoteaux M, Garyfallidis E, Gur Y, Lin YC, et al. Quantitative Comparison of Reconstruction Methods for Intra-Voxel Fiber Recovery From Diffusion MRI. IEEE Trans Med Imaging 2014;33:384-99.
27. Aranda R, Ramirez-Manzanares A, Rivera M. Sparse and Adaptive Diffusion Dictionary (SADD) for recovering intra-voxel white matter structure. Med Image Anal 2015;26:243-55.
28. Sperl JI, Sprenger T, Tan ET, Menzel MI, Hardy CJ, Marinelli L. Model-based denoising in diffusion-weighted imaging using generalized spherical deconvolution. Magn Reson Med 2017;78:2428-38.
29. Sneag DB, Zochowski KC, Tan ET, Queler SC, Burge A, Endo Y, Lin B, Fung M, Shin J. Denoising of diffusion MRI improves peripheral nerve conspicuity and reproducibility. J Magn Reson Imaging 2020;51:1128-37.
30. Neuman CH. Spin echo of spins diffusing in a bounded medium. J Chem Phys 1974;60:4508-11.
31. van Gelderen P, Despres D, Vanzijl PCM, Moonen CTW. Evaluation of Restricted Diffusion in Cylinders. Phosphocreatine in Rabbit Leg Muscle. J Magn Reson B 1994;103:255-60.
32. Tan ET, Wilmes LJ, Joe BN, Onishi N, Arasu VA, Hylton NM, Marinelli L, Newitt DC. Denoising and Multiple Tissue Compartment Visualization of Multi-b-Valued Breast Diffusion MRI. J Magn Reson Imaging 2021;53:271-82.
33. Heemskerk AM, Damon BM. Diffusion Tensor MRI Assessment of Skeletal Muscle Architecture. Curr Med Imaging Rev 2007;3:152-60.
34. Sacolick LI, Wiesinger F, Hancu I, Vogel MW. B1 mapping by Bloch-Siegert shift. Magn Reson Med 2010;63:1315-22.
35. Tan ET, Marinelli L, Slavens ZW, King KF, Hardy CJ. Improved correction for gradient nonlinearity effects in diffusion-weighted imaging. J Magn Reson Imaging 2013;38:448-53.
36. Sumpf TJ, Petrovic A, Uecker M, Knoll F, Frahm J. Fast T2 Mapping with Improved Accuracy Using Undersampled Spin-Echo MRI and Model-Based Reconstructions with a Generating Function. IEEE Trans Med Imaging 2014;33:2213-22.
37. Liu CY, McKenzie CA, Yu H, Brittain JH, Reeder SB. Fat quantification with IDEAL gradient echo imaging: Correction of bias from T1 and noise. Magn Reson Med 2007;58:354-64.
38. Klein S, Staring M, Murphy K, Viergever MA, Pluim JPW. elastix: a toolbox for intensity-based medical image registration. IEEE Trans Med Imaging 2010;29:196-205.
39. Wall BT, Dirks ML, Loon LJC van. Skeletal muscle atrophy during short-term disuse: Implications for age-related sarcopenia. Ageing Res Rev 2013;12:898-906.
40. Argadine HM, Hellyer NJ, Mantilla CB, Zhan WZ, Sieck GC. The effect of denervation on protein synthesis and degradation in adult rat diaphragm muscle. J Appl Physiol 2009;107:438-44.
41. Ploutz-Snyder LL, Nyren S, Cooper TG, Potchen EJ, Meyer RA. Different effects of exercise and edema on T2 relaxation in skeletal muscle. Magn Reson Med 1997;37:676-82.
42. Patten C, Meyer RA, Fleckenstein JL. T2 Mapping of Muscle. Semin Musculoskelet Radiol 2003;7:297-305.
43. Alexander DC. A General Framework for Experiment Design in Diffusion MRI and Its Application in Measuring Direct Tissue-Microstructure Features. Magn Reson Med 2008;60:439.
44. Sneag DB, Mendapara P, Zhu JC, Lee SC, Lin B, Curlin J, Bogner EA, Fung M. Prospective respiratory triggering improves high-resolution brachial plexus MRI quality. J Magn Reson Imaging 2019;49:1723-9.
45. Karampinos DC, King KF, Sutton BP, Georgiadis JG. Myofiber Ellipticity as an Explanation for Transverse Asymmetry of Skeletal Muscle Diffusion MRI In Vivo Signal. Ann Biomed Eng 2009;37:2532.
46. Breckwoldt MO, Stock C, Xia A, Heckel A, Bendszus M, Pham M, Heiland S, Bäumer P. Diffusion Tensor Imaging Adds Diagnostic Accuracy in Magnetic Resonance Neurography. Invest Radiol 2015;50:498-504.

Cite this article as: Tan ET, Zochowski KC, Sneag DB. Diffusion MRI fiber diameter for muscle denervation assessment. Quant Imaging Med Surg 2022;12(1):80-94. doi: 10.21037/qims-21-313

Appendix 1 Forward model with cylindrical, restricted diffusivity muscle model

Following the signal equation of normalized diffusivity signal S_i from intracellular muscle $S_{M,i}$ and extracellular fluid, $S_{F,i}$ from eq. [1], $S_{M,i}$ is defined radially as an infinite cylinder with impermeable transverse boundaries and axially with Gaussian diffusivity $D_{//}$, where r is the cylinder radius, gradient vector $\vec{g}$, and the pulse width δ and mixing time Δ. By accounting for its radial gradient magnitude $g_{\perp}^2$ and axial gradient magnitude $g_{//}^2$, the natural logarithm of $S_{M,i}$ can be expressed as a summation of radial and axial terms. The radial term is derived from Neuman(30), and includes terms for the intracellular water diffusivity D_0 and α_m^2, which is the m-th root of the derivative of the Bessel function J such that $J'_1(\alpha_m^2 r)=0$:

$$\ln\left[S_{M,i}\left(r,\vec{g},\delta,\Delta\right)\right]=-2\gamma^2 g_{\perp}^2\sum_{m=1}^{\infty}\frac{2\delta/\alpha_m^2 D_0-\left(2+e^{-\alpha_m^2 D_0(\Delta-\delta)}-2e^{-\alpha_m^2 D_0\delta}-2e^{-\alpha_m^2 D_0\Delta}+e^{-\alpha_m^2 D_0(\Delta+\delta)}\right)/\left(\alpha_m^2 D_0\right)^2}{\alpha_m^2\left(\alpha_m^2 r^2-2\right)}-\gamma^2 g_{//}^2\delta^2\left(\Delta-\frac{\delta}{3}\right)D_{//} \quad [1]$$

While $S_{F,i}$ is defined as:

$$\ln\left[S_{F,i}\left(\vec{g},\delta,\Delta\right)\right]=-\gamma^2\vec{g}^2\delta^2\left(\Delta-\frac{\delta}{3}\right)D_F. \quad [2]$$

Appendix 2 Multi-compartment model

For K_{Res}×N_{Res} anisotropic, K_{Hin} isotropic, K_{Fre} isotropic and K_{Noise} isotropic tissue compartments, each with $f_{Res,j,n}$, $f_{Hin,k}$, $f_{Fre,k}$, $f_{Fat,k}$, compartment fractions, the sum of each tissue is defined by:

$$f_{Res}=\sum_{j=1}^{K_{Res}}\sum_{n=1}^{N_{Res}}f_{Res,j,n} \quad [3]$$

$$f_{Hin}=\sum_{k=1}^{K_{Hin}}f_{Hin,k} \quad [4]$$

$$f_{Fre}=\sum_{k=1}^{K_{Fre}}f_{Fre,k} \quad [5]$$

$$f_{Fat}=\sum_{k=1}^{K_{Noise}}f_{Fat,k} \quad [6]$$

Each of the anisotropic compartments has pre-defined axial/parallel and radial/orthogonal diffusivities ($\lambda_{//}$, $\lambda_{\perp}$), whereas each of the isotropic compartments has solely a mean diffusivity (λ) defined. For a maximum b-value, b and for each normalized gradient vector $\vec{q}$, radial vector $\vec{u}$ and the model's signal estimate ($\hat{s}$) is defined as

$$\begin{aligned}\hat{s}\left(b,\vec{q}\right)=&\sum_{j=1}^{K_{Res}}\sum_{n=1}^{N_{Res}}f_{Res,j,n}\exp\left(-\left(\lambda_{||,j}b\left(\vec{q}^T\vec{u}_n\right)^2\right)\left(\lambda_{\perp,j}b\left(1-\left(\vec{q}^T\vec{u}_n\right)^2\right)\right)\right)\\&+\sum_{k=1}^{K_{Hin}}f_{Hin,k}\exp\left(-\lambda_{Hin,k}b\right)+\sum_{k=1}^{K_{Fre}}f_{Fre,k}\exp\left(-\lambda_{Fre,k}b\right)+\sum_{k=1}^{K_{Fat}}f_{Fat,k}\exp\left(-\lambda_{Fat,k}b\right)\end{aligned} \quad [7]$$

To adapt the method for multi-b-valued muscle diffusion, where tissue anisotropy would be less than that in the brain and where fewer diffusion-encoding directions would typically be used, a model with far fewer compartments and fewer directionalities was proposed. In multi-b-valued acquisition, b-values smaller than the maximum b-value were created by q-vectors with a squared magnitude less than one. The composition of the compartments and optimization parameter values are listed in *Table 1*. A wide range of assumed fractional anisotropy (0.11-1.00) was used in the restricted compartments to account for the wide range of FA observed in the literature.

https://dx.doi.org/10.21037/qims-21-313

Appendix 3 Precision and bias error

Propagation of variance was used to convert units from each metric $M \in \{f_{Res}, f_{Hin}, f_{Fre}, f_{Fat}, \text{MD}, \text{AD}, \text{RD}, \text{FA}\}$ to that of r, using the derivative, $\frac{\partial M(r)}{\partial r}$. Precision error $\varepsilon_{M,n}$ for a given metric and simulation n was defined as the root-mean-square of the metric variance $\sigma^2_{M,n}(r)$ summed across all r values:

$$\varepsilon_{M,n} = \frac{\sqrt{\sum_r^{N_r} \sigma^2_{M,n}(r)}}{\sum_r^{N_r} \left| \frac{\partial M(r)}{\partial r} \right|} \quad [8]$$

The bias error, $\beta_{M,N}$, followed the same approach, except that bias was defined as the error resulting from varying one parameter, N, which was either SNR, ρ, D_0 or $D_{//}$, keeping other parameters constant. To compute bias, the metric variance, $\sigma^2_{M,N}(r)$ was defined as that from one of the parameters SNR, ρ, D_0 or $D_{//}$:

$$\beta_{M,N} = \frac{\sqrt{\sum_r^{N_r} \sigma^2_{M,N}(r)}}{\sum_r^{N_r} \left| \frac{\partial M(r)}{\partial r} \right|} \quad [9]$$

https://dx.doi.org/10.21037/qims-21-313